



Deformable Registration of MRA Images with 4D Flow Images to Facilitate Accurate Estimation of Flow Properties within Blood Vessels

Dan U. Lior^{a,*}, Charles Puelz^a, Justin Weigand^a, Kristina V. Montez^b, Yimo Wang^c, Silvana Molossi^a, Daniel J. Penny^a, Craig G. Rusin^a

^aDepartment of Pediatrics, Division of Cardiology, Baylor College of Medicine and Texas Children's Hospital, Houston, U.S.A.

^bSchool of Engineering Medicine, Texas A&M University, Houston, U.S.A.

^cDepartment of Computational Applied Mathematics and Operations Research, Rice University, Houston, U.S.A.

ARTICLE INFO

Article history:

Keywords: registration, centerlines, MRA, 4D Flow

ABSTRACT

Patients with congenital and acquired heart conditions often undergo studies using Magnetic Resonance Angiography (MRA) images and time-resolved four-dimensional phase-contrast magnetic resonance (4D Flow) images to noninvasively estimate blood flow properties such as flux¹, wall shear stress² and vorticity³. The 4D Flow image specifies velocity of blood within the imaging volume while the MRA image yields, via segmentation, an accurate representation of the geometry of the vessel walls. Both the geometry of the vessel walls and the velocity of the blood within them are required to generate accurate estimates of vessel flow properties. The images are not acquired simultaneously so the patient is subject to shifting between scans, resulting in misalignment of the images. Additionally, motion from the respiratory and cardiac cycles causes deformation within the anatomical structures themselves. This misalignment and deformation causes inaccuracy in estimates of blood flow properties. An approach is presented that partially alleviates these discrepancies thus facilitating more accurate estimation of blood flow properties.

© 2023 Elsevier B. V. All rights reserved.

1. Introduction

1.1. Background

Understanding the relationship between geometry and flow properties through major blood vessels has important clinical implications, especially in the treatment of heart disease. For example, surgical reconstruction of the aorta in single ventricle physiology alters vessel morphology and confers disturbed flow patterns. In turn, altered flow may affect single ventricle function, hemodynamics, and clinical outcomes Fogel et al. (2014); Biglino et al. (2012, 2014); Biko et al. (2019); Schäfer

et al. (2019); Bruse et al. (2017); Taylor-LaPole et al. (2023). In general, analysis of flow properties in complex physiology resulting from congenital heart disease can be used to assess both disease severity and surgical success.

Vessel geometries may be measured using magnetic resonance angiography (MRA), and blood velocities may be measured using time-resolved phase-contrast cardiac magnetic resonance (4D Flow) imaging. Performing these imaging sequences separately can result in misaligned velocity and geometry information and hence may lead to inaccurate assessment of flow properties. Reconciling the velocity and geometry data via a technique that registers these sequences may best localize flow perturbations in vessels of clinical interest.

*Corresponding author:
e-mail: dan.lior@bcm.edu, sitiposit@gmail.com (Dan U. Lior)

1.2. The Main Registration Problem

Routinely, an MRA image and a corresponding 4D Flow image are acquired from a patient by the same machine in close succession, but not simultaneously. Shifting of the patient and motion from the respiratory and cardiac cycles that occurs between scans results in misalignment of the images. This misalignment is a source of inaccuracy in subsequent computation of flow properties which combines information gleaned from both images. In order to reduce this source of inaccuracy in the computed flow properties, a method is presented to construct a *corrected* MRA image that more closely aligns with the corresponding 4D Flow image.

Figure 1 depicts the aortic wall as extracted from the uncorrected MRA and from the MRA registered using methods to be described in this paper. The improved alignment with the 4D flow image is apparent from the intersection of these surfaces with a planar section of the speed field (i.e. magnitude of velocity) generated from the 4D flow image.

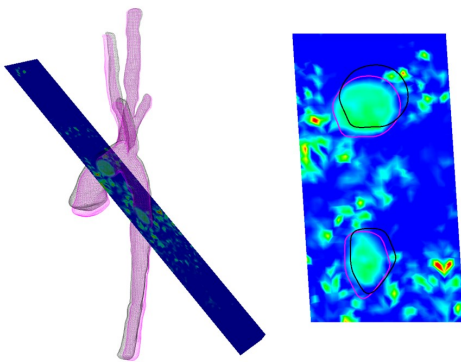


Fig. 1. Cross section of speed field from 4D Flow image with vessels extracted from the original (grey) and the registered (magenta) MRA images.

Registration is a common theme in image processing tasks. A *registration problem* calls for a transformation of a given *floating* object whose image aligns with a given *fixed* object.

In the present context, the floating object is the uncorrected MRA image, the fixed object is the 4D Flow image and the transformation is a displacement field $\Psi: \mathbb{R}^3 \rightarrow \mathbb{R}^3$. The corrected MRA image is the result of applying⁴ Ψ to the uncorrected MRA image. Various criteria for “alignment” are given in the results section (Section 4).

In more technical language, the main registration problem addressed in this paper is a feature-based⁵, multimodal⁶, deformable⁷ registration of an MRA image to a 4D Flow image.

1.3. Prior Work

Algorithms for registering 4D Flow images to scalar images (e.g. MRA images) have been published. Gupta et al.

(2018) registered multi-slice balanced steady-state precession magnetic resonance images to 4D Flow images. A sequence of 2D rigid transformations on the slices of the former image were computed and an optimal representative selected according to a cost function. Sabokrohiyeh et al. (2019) focused on improving localization, a particular aspect of the registration algorithm in Gupta et al. (2018). While the resulting registration transformation was not necessarily rigid, it was given by a transformation matrix and hence affine. Sang et al. (2022, 2021) presented a deep learning approach in which a motion representation model was trained using 10 multi-detector computed tomography coronary angiography images. Bustamante et al. (2015) used an atlas to automatically segment 4D Flow images. Registration was a part of the underlying construction, but registration of MRI to 4D Flow images was not in the scope of their paper.

Here, a novel approach to this registration problem is presented. For vessels of interest that are represented in both images, centerlines are extracted. A novel curve registration algorithm is used to simultaneously register each centerline extracted from the MRA image with its corresponding centerline extracted from the 4D Flow image. A smooth displacement map Ψ represented by a Cartesian grid of B-spline functions is calibrated to approximately extend the centerline registration transformation. The corrected MRA image is given by the composition of Ψ with the original MRA image (See Figure 1).

Unlike the approaches of Gupta et al. (2018) and Sabokrohiyeh et al. (2019), the resulting registration (i.e. the displacement field) is not restricted to an affine map, and in particular not a rigid map. Deformations of internal organs during the cardiac and respiratory cycles are certainly not affine, so the added flexibility of a non-rigid deformation field affords more accurate registration.

Unlike the machine learning approaches of Sang et al. (2022) and Bustamante et al. (2015), the current method is not limited by the relatively small class of images used to train the underlying neural network. This is of particular importance for the intended application to patients with abnormal morphology resulting from congenital heart disease.

1.4. Data Source and Collection

The MRA and 4D Flow images used to test the methods in this paper come from a single patient with a Fontan circulation. Data was acquired at Texas Children’s Hospital under protocol H-46224: “Four-Dimensional Flow Cardiovascular Magnetic Resonance for the Assessment of Aortic Arch Properties in Single Ventricle Patients” approved by the Baylor College of Medicine Institutional Review Board.

1.5. Organization

The solution presented in this paper to the main registration problem requires the registration of certain curves extracted from MRA and 4D Flow images. Registration algorithms for such curves are presented in section 2. The main registration algorithm for MRA to 4D Flow images is presented in section 3. The results section (Section 4) evaluates the alignment achieved by the registration algorithm applied to a pair of real MRA and

⁴Exactly how a displacement field transforms an MRI image is described in the following sections.

⁵the features being centerlines of vessels

⁶The “mode” of a 4D Flow image is a vector field representing velocity whereas the mode of an MRA image is a scalar field representing water content

⁷ Ψ is not required to be rigid or even affine; it can include complex local variation.

4D Flow images. The conclusion section (Section 5) includes a discussion of limitations and future work.

2. Registration of Curves

2.1. Polylines

A *polyline* is a list of points in \mathbb{R}^n for some fixed positive integer n . \mathcal{P}^n denotes the set of polylines in \mathbb{R}^n . For a real positive number h , \mathcal{P}_h^n denotes the set of polylines in \mathcal{P}^n having constant distance h between consecutive vertices. Such polylines are called *uniform polylines*.

For any parameterized curve

$$\gamma : [0, 1] \rightarrow \mathbb{R}^n$$

and any h , the canonical polyline $\gamma_h \in \mathcal{P}_h^n$ approximating γ is given by

$$\gamma_h := \gamma(t_0), \dots, \gamma(t_k)$$

where

$$0 = t_0 < t_1 < \dots < t_k \leq 1$$

is the unique maximal set of real numbers satisfying

$$|\gamma(t_i) - \gamma(t_{i-1})| = h, \quad 1 \leq i \leq k$$

2.1.1. Differential Measures of Polylines

Differential measures of curves such as tangents, curvature and torsion are central to the motivation and implementation of curve registration algorithms. Clearly, polylines fail all but C^0 smoothness conditions, so they do not admit such measures⁸. However, the literature on discrete differential geometry contains simple and efficient algorithms that compute, directly from uniform polyline approximations to γ , discrete approximations of such differential measures, e.g. Langer *et al.* (2005).

2.1.2. Transformations of Polylines

A *transformation* of a polyline is a specification of displacement for each vertex on the polyline. The *closest step* σ from one polyline P towards a polyline Q is the transformation of P that sends each vertex \mathbf{u} of P to the closest vertex $\sigma(\mathbf{u})$ of Q . The *closest projection* π from one polyline P towards a polyline Q is the transformation of P that sends each vertex \mathbf{u} of P to the perpendicular projection of \mathbf{u} onto the tangent line at $\sigma(\mathbf{u})$.

Both the closest step and the closest projection are designed to move P closer to Q , but the closest projection tends to preserve the length and shape of P better than the closest step, especially when P and Q differ significantly in length. See Figure 2.

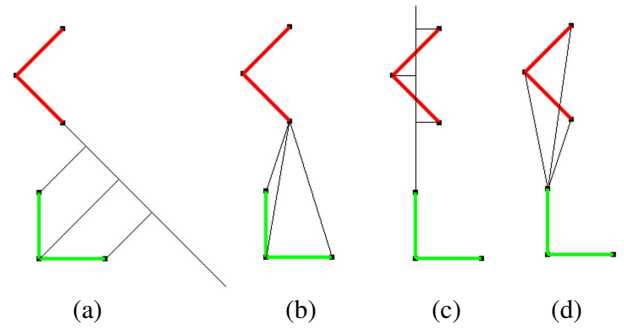


Fig. 2. (a) Closest projection of green to red polyline, (b) closest step of green to red polyline, (c) closest projection of red to green polyline, (d) closest step of red to green polyline

2.1.3. Distance Histograms

Let p, q be polylines and let σ and π denote the closest step transformation and the closest projection transformation from P toward Q . Let V be the ordered set of vertices of P , let W denote the range of σ and let V_0 be the subset of V obtained by replacing, for each $\mathbf{w} \in W$, each interval of $\sigma(\mathbf{w}) \subset V$ with a representative of minimal distance to \mathbf{w} . The histogram of the set:

$$\{\|\mathbf{v} - \pi(\mathbf{v})\| : \mathbf{v} \in V_0\}$$

is the *reduced asymmetric distance histogram* from P to Q . Note that this histogram is not necessarily the same as the reduced asymmetric distance histogram from Q to P .

Formal metrics on \mathcal{P}^n exist (e.g., the Hausdorff metric) but a more informative measure of the discrepancy between polylines in the present context is the pair of reduced asymmetric distance histograms between P and Q . These histograms play a role in the evaluation of registrations (See Section 4).

2.2. Registration of Polylines and Polyline Networks

2.2.1. Rigid Registration of Polylines

A rigid polyline transformation T is the restriction of some⁹ rigid map of the ambient Euclidean space. The algorithm presented below for the rigid registration of polylines is a variant of the well-known iterated closest point algorithm Besl and McKay (1992). At each iteration, a rigid transformation is computed which, when composed with the rigid transformations from the previous iterations, brings the floating polyline closer to the fixed polyline. The algorithm halts on convergence¹⁰ or when the number of iterations exceeds a prescribed value. The reported rigid transformation is the composition of all the incremental rigid transformations.

The procedure for computing each incremental rigid transformation T is as follows:

⁸It is possible that a curve admits exact calculation of differential quantities. In that case, the polyline can inherit this differential information at its vertices. These values are, however, invalidated when the polyline undergoes nonrigid transformation.

⁹In all but trivial cases, this map is unique.

¹⁰Convergence is determined by an upper bound (specified as a parameter of the algorithm) of the Frobenius norm of the matrix representing the incremental affine transformation.

1. The closest step σ and the closest projection π from the floating polyline to the fixed polyline are computed.
2. For fixed parameters α, β, γ of the algorithm, the domains of σ and π are restricted to a subset I of their original domain (the vertices of the current intermediate floating polyline). The elements $\mathbf{u} \in I$ are selected so that:
 - The angle between the tangent line of the floating polyline at \mathbf{u} that of the fixed polyline at $\sigma(\mathbf{u})$ is bounded by a threshold α .
 - The absolute difference between the curvature of the floating polyline at \mathbf{u} and that of the fixed polyline at $\sigma(\mathbf{u})$ is bounded by a threshold β .
 - The absolute difference between the torsion of the floating polyline at \mathbf{u} and that of the fixed polyline at $\sigma(\mathbf{u})$ is bounded by a threshold γ .
3. The rigid transformation, T , that maps the points $\mathbf{u} \in I$ as close as possible to their corresponding points $\pi(\mathbf{u})$, is computed. As long as the points $\mathbf{u} \in I$ are not collinear, the transformation is unique and can be readily computed as the solution of the well-known ‘‘Procrustes problem’’.

Note that the image of the floating polyline is not expected to match the fixed polyline in its entirety. Restricting the domain of σ and π to I localizes the incremental matching procedure.

2.2.2. Nonrigid Registration of Polylines

The nonrigid transformation of the floating polyline X is generated as a composition of incremental transformations that brings the floating polyline progressively closer to the fixed polyline. A mode parameter specifies one of three available variants of the incremental transformation. The stopping criteria of the iterative process is also determined by this mode. In all modes, the procedure for generating each incremental non-rigid transformation T begins with the computation of the closest step σ and closest projection π . Subsequent steps of the incremental procedure depend both on the mode and on parameters $\epsilon > 0$ and $0 < \mu < 1$. Higher values of μ increase the speed of convergence but also reduce the chance of successful convergence. The parameter ϵ is used as a threshold for determining convergence of the iterative process.

Mode 1: For each vertex \mathbf{u} of X ,

$$T(\mathbf{u}) := (1 - \mu)\mathbf{u} + \mu\pi(\mathbf{u})$$

The stopping criteria consists of a maximum iteration bound and the convergence condition:

$$\max_{\mathbf{u}} \|T(\mathbf{u}) - \pi(\mathbf{u})\| < \epsilon$$

Mode 2: The images of the vertices of X under T form the solution of a certain linear system constrained by: For each vertex \mathbf{u} of X ,

- $T(\mathbf{u})$ is on the line between \mathbf{u} and $\pi(\mathbf{u})$
- $\theta(T(\mathbf{u}), \sigma(\mathbf{u})) = \mu\theta(\mathbf{u}, \sigma(\mathbf{u}))$, where $\theta(\mathbf{p}, \mathbf{q})$ denotes the angle between the tangent lines at \mathbf{p} and \mathbf{q} .

The stopping criterion consists of a maximum iteration bound and the convergence condition:

$$\max_{\mathbf{u}} |\theta(\mathbf{u}, \sigma(\mathbf{u}))| < \epsilon$$

Mode 3: The $T(X)$ is the polyline satisfying: For each vertex \mathbf{u} of X ,

- $\kappa(T(\mathbf{u})) = (1 - \mu)\kappa(\mathbf{u}) + \mu\kappa(\sigma(\mathbf{u}))$
- $\tau(T(\mathbf{u})) = (1 - \mu)\tau(\mathbf{u}) + \mu\tau(\sigma(\mathbf{u}))$
- $|\mathbf{c} - \mathbf{c}_2| = \mu|\mathbf{c}_1 - \mathbf{c}_2|$

Here κ denotes curvature, τ denotes torsion, and $\mathbf{c}, \mathbf{c}_1, \mathbf{c}_2$ denote, respectively, the centroids of the polylines $T(X), \pi(X)$ and X . The stopping criterion consists of a maximum iteration bound and the convergence condition:

$$|\mathbf{c} - \mathbf{c}_2| < \epsilon$$

2.2.3. Polyline Networks and their Registration

A *polyline network* is a list of polylines in \mathcal{P}_h^n for some fixed values of n and h . There is no assumed or required relation between the polylines of such a network. In particular, while polylines in a network may intersect (themselves or each other) the intersection points are not distinguished or specified. The algorithm presented for the registration of polyline networks is essentially the simultaneous application of the rigid registration and deformable registration algorithms to the constituent polylines of the network.

The closest step transformation of polylines can be extended *blindly* or *informedly* to the context of polyline networks. The *blind* closest step transformation is a direct analogue of the closest step transformation in single polyline case. Namely, for a vertex \mathbf{u} of the floating polyline network, $\sigma(\mathbf{u})$ is taken to be the vertex in the fixed polyline network closest to \mathbf{u} . To define the *informed* closest step transformation, a correspondence

$$g : \{1, 2, \dots, m\} \rightarrow \{1, 2, \dots, n\}$$

is provided between the polylines (c_1, \dots, c_m) of the floating network and the polylines (d_1, \dots, d_n) of the fixed network. Then, for a vertex \mathbf{u} of the polyline c_i , $\sigma(\mathbf{u})$ is taken to be the closest point to \mathbf{u} on the polyline $d_{g(i)}$.

The overall polyline network registration algorithm begins with the computation of the closest step and closest projection transformations (in blind or informed mode, as specified by an algorithm parameter) for a given pair $X_{floating}, X_{fixed}$ of polyline networks.

Next, a rigid polyline transformation L is generated by the rigid registration of $X_{floating}$ to X_{fixed} . Finally, a polyline transformation T of $L(X_{floating})$ is generated by the nonrigid registration of $L(X_{floating})$ to X_{fixed} . The final registered polyline network is given simply by the composition $T \circ L$.

If the polyline network registration is successful then, for each vertex \mathbf{q} of $L(X_{floating})$, $T(\mathbf{q})$ lies near a point on the fixed centerline network corresponding to the vertex $L^{-1}(\mathbf{q})$ on the floating centerline network. See Figure 3.

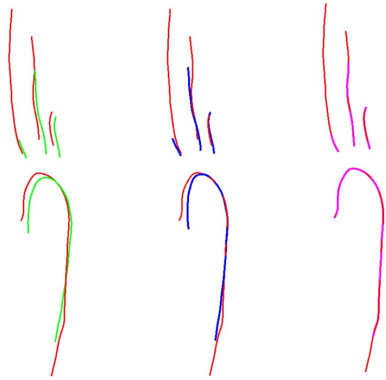


Fig. 3. Polyline networks X_{fixed} (red), $X_{floating}$ (green), $L(X_{floating})$ (blue) and $T(L(X_{floating}))$ (magenta)

3. Registration of MRA Images to 4D Flow Images

An MRA image is represented by a sequence of scalar-valued functions:

$$\rho_i: U \subset \mathbb{R}^3 \rightarrow \mathbb{R}$$

Here, U is a regular rectangular lattice and each function ρ_i , referred to here as a *frame*, corresponds to measurements made at each node of U at a particular instant of time specified by the index i .

A 4D Flow image is represented by two sequences:

$$\mathbf{v}_j: V \subset \mathbb{R}^3 \rightarrow \mathbb{R}^3, \quad \mu_j: W \subset \mathbb{R}^3 \rightarrow \mathbb{R}$$

Here, V, W are regular rectangular lattices and each frame \mathbf{v}_j (resp. μ_j) corresponds to measurements made at each node of V (resp. W) at a particular instant of time specified by the index j . The measurements represented by ρ_i and μ_j can be understood as densities and the measurements represented by \mathbf{v}_j can be understood as velocities. The frame indices represent uniformly spaced instances in time. In the 4D Flow image, these times span a single cardiac cycle while in the MRA image they occur in the same instant of a cardiac cycle over several cycles.

While ρ_i , \mathbf{v}_j and μ_j are only specified on discrete sets of points (i.e. the nodes of lattices), they are extended bilinearly to the (box-shaped) convex hulls of those sets, denoted \widehat{U} , \widehat{V} and \widehat{W} .

The two ingredients \mathbf{v}_j and μ_j of the 4D Flow image are assumed to be *aligned*. That is, $\mathbf{v}_j(\mathbf{p})$ and $\mu_j(\mathbf{p})$ are the velocity and density (respectively) at \mathbf{p} , for any point \mathbf{p} in their common extended domain.

The 4D Flow image and the MRA image are typically not aligned; $\mathbf{v}_j(\mathbf{p})$ and $\rho_i(\mathbf{p})$ are the velocity and density at distinct (but nearby) points.

The registration problem is to find a displacement map

$$\Psi: \mathbb{R}^3 \rightarrow \mathbb{R}^3$$

so that the corrected MRA image $\rho_i \circ \Psi$ aligns¹¹ with the 4D Flow image.

3.1. Vessels and Centerlines

A *vessel* is a connected surface whose boundary has exactly two components (an inlet and an outlet) and whose cross sections perpendicular to a certain directed curve, its *centerline*, are approximately circular. Under modest smoothness conditions, a sufficiently narrow and circular vessel is well-approximated by its centerline. Similarly, a smooth transformation of such a vessel is well-approximated by a transformation of its centerline. These observations motivate the main registration algorithm presented in Section 3.

3.2. Image Enhancement

For both MRA and 4D Flow images, different (parts of) vessels in the circulation system are better reflected in different frames. For example, the frames of the 4D Flow image corresponding to the systolic phase of the cardiac cycle highlight the aorta, while frames later in the cycle better highlight the pulmonary arteries. In the case of the MRA image, higher frame indices correspond to larger elapsed times from initial injection of a contrast agent. As such, vessels immediately downstream of the injection site are more apparent in lower indexed frames than the vessels further downstream.

An *enhanced* MRA image is obtained by summing a selection I of frames:

$$\rho := \sum_{i \in I} \rho_i$$

Similarly, an enhanced 4D Flow is obtained by summing a section J of frames:

$$\mathbf{v} := \sum_{j \in J} \mathbf{v}_j \quad \mu := \sum_{j \in J} \mu_j$$

The frame selections I, J are made by the user as an initial step in the registration algorithm. Heuristically, I and J are selected large enough to highlight all the relevant vessels of interest in both images but no larger, so as not to introduce excessive blurring that results from adding images of a shifting/deforming object.

3.3. Extraction of Vessels and their Centerlines from Scalar Images

Freely available software (e.g., 3D Slicer Kikinis et al. (2013), SimVascular Updegrave et al. (2017)) facilitates the segmentation¹² of vessel surfaces from scalar fields such as MRA and Computed Tomography (CT) images. The same software also facilitates the extraction of centerlines from those vessel surfaces or directly from the scalar field.

3.4. Scalarizing a 4D Flow Image

Unlike MRA and CT, 4D Flow images are not scalar fields so this method of extraction does not directly apply. What is required is a method to extract a scalar image from a 4D Flow image to which the software mentioned above can be applied.

¹¹Criteria for “aligns” are presented in Section 4.

¹²The term *segmentation* refers to the process and the end result of extracting a surface mesh from a scalar field.

One obvious method is to simply take the speed (i.e. magnitude of velocity) image, the result of which is an image of the fluid speed. A second method is to replace the 4D Flow image with its companion “magnitude” image¹³. A final method is to apply the *coherence* operator, as described below.

For a given vector field \mathbf{v} , the *coherence* at a point $\mathbf{p} \in \mathbb{R}^3$ measures the discrepancy between the direction of \mathbf{p} and the direction of \mathbf{q} for nearby points \mathbf{q} . More precisely:

$$\text{coherence}(\mathbf{p}) := 1 - \lim_{\epsilon \rightarrow 0} \frac{\int_{B_\epsilon(\mathbf{p})} \cos \theta_{\mathbf{p}}}{|B_\epsilon|} \quad (1)$$

In the discretized version of coherence, \mathbb{R}^3 is replaced with a grid of points \mathbf{p}_i and the second term above is replaced with an average value of $\cos \theta_{\mathbf{p}}$ over voxels adjacent to \mathbf{p} .

Figure 4 shows slices of the scalar images obtained from a sample 4D Flow image using these three methods. In this particular case, it is apparent that the coherence captures the vessel wall most accurately. In fact, this was apparent in all other slices and 4D Flow images that were examined.

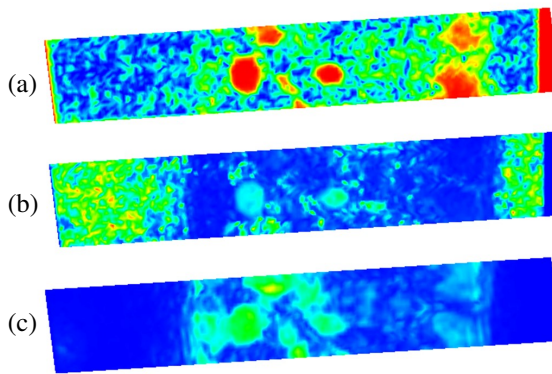


Fig. 4. Slice of a 4D Flow image (same slice as in Figure 1) scalarized by (a) coherence, (b) speed, and (c) magnitude

Despite being superior to two alternate methods presented above for “scalarizing” a 4D Flow image, surfaces extracted from coherence images suffer from inaccuracy, bias and incompleteness. The inaccuracy results from the relatively coarse spatial resolution of the 4D Flow image compared to resolutions of CT or MRA images. Segmentations of coherence images represent the boundary between high and low fluid velocities. Due to the no-slip condition, this boundary invariably occurs strictly inside the vessel wall, thus introducing a bias in the segmented surfaces. Since the 4D Flow signal only detects sufficiently high fluid velocity, some vessels are only visible in certain intervals of the cardiac cycle and some vessels (exhibiting little to no flow) are entirely unrepresented in the 4D Flow image. However, centerlines extracted from the coherence image are resilient to the noise and bias that plagues segmentations of vessel surfaces from coherence images.

¹³The velocity field of a 4D Flow image is reconstructed from the phase information of the MRI return signal, while a scalar attribute called “magnitude” is included in 4D Flow images which roughly corresponds to tissue density.

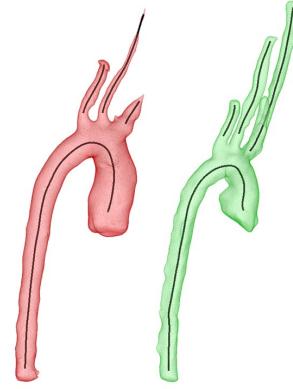


Fig. 5. Vessel surfaces and centerlines extracted from 4D Flow coherence (red) and MRA (green) images

3.5. Constructing the Displacement Field from the Polyline Network Registration

Centerlines are extracted from both the MRA and 4D Flow image, for each vessel of interest. These centerlines are registered using the polyline network registration algorithm described in section 2.

Typically, vessels represented in the 4D Flow image are entirely represented in the corresponding MRA image, while corresponding vessels represented in the MRA image are often only partially detectable or completely undetectable in the 4D Flow image. This phenomenon is related to the incompleteness of 4D Flow images discussed in a previous section. As a result, the centerlines of 4D Flow networks tend to be shorter than their corresponding centerlines in the MRA networks. Considering the inherent asymmetry of the polyline registration algorithms regarding the roles of the fixed vs floating objects, it is preferable that the centerline network extracted from the MRA image assumes the role of the fixed object and that the centerline network extracted from 4D Flow image assume the role of the floating object.

Recall that the centerline network registration is a composition $T \circ L$ where L is a rigid transformation. Note that this map is formally only defined on the vertices of the centerline network obtained from the MRA image. The displacement map Ψ approximately extends this composition to a smooth map of \mathbb{R}^3 .

The extension, \widehat{L} , of the rigid transformation L to \mathbb{R}^3 , is determined from the rigid transformation. On the other hand, the extension of T to \mathbb{R}^3 is far from unique. A construction is presented below for a map $\widehat{T}: \mathbb{R}^3 \rightarrow \mathbb{R}^3$ which approximately extends T . The desired displacement field Ψ is then simply given by the composition $\Psi = \widehat{T} \circ \widehat{L}$.

\widehat{T} is a linear combination of several translates of a certain B-spline function. The coefficients of this linear combination form the solution to an optimization problem. An illustration of \widehat{T} taken from a sample registration appears in Figure 6.

Let $\phi: \mathbb{R} \rightarrow \mathbb{R}$ denote the B-spline of degree d centered at 0. Then ϕ is C^{d-1} , piecewise polynomial of degree d , and has radius of support $r_s = (d + 1)/2$. For example, if $d = 3$ then $r_s = 2$ and the graph of $\phi(t)$ is illustrated in Figure 7.

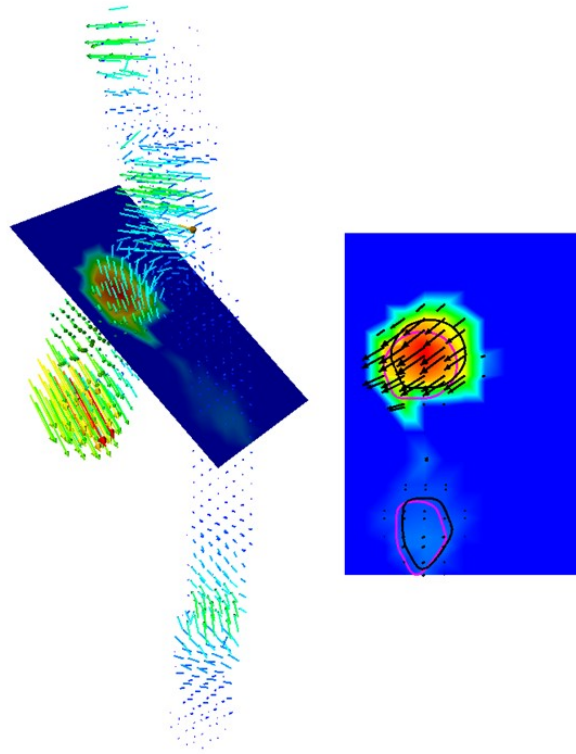


Fig. 6. The displacement field \widehat{T} extending the nonrigid polyline registration transformation. The curves in the cross-section depict vessels segmented from the unregistered (grey) and registered (magenta) MRA images.

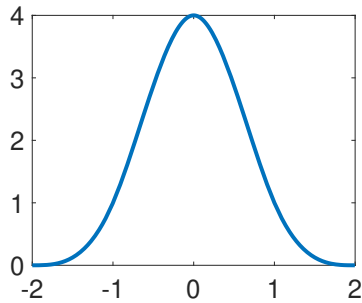


Fig. 7. Centered Cubic B-Spline ϕ

The function

$$\begin{aligned} \Phi: \mathbb{R}^3 &\rightarrow \mathbb{R} \\ (x, y, z) &\mapsto \phi(x)\phi(y)\phi(z) \end{aligned}$$

and each of its translates are C^{d-1} and have radius of support $r_s = (d + 1)/2$ with respect to the Manhattan metric (a.k.a the l_1 metric) on \mathbb{R}^3 . In particular, let $\Phi_{i,j,k}$ denote a translate of Φ to the $(i, j, k)^{th}$ node of an $n_I \times n_J \times n_K$ integer lattice. Each linear combination $\sum_{i,j,k} \alpha_{i,j,k} \Phi_{i,j,k}$ is also C^{d-1} and its value at any point is determined entirely by the value of a fixed number of these translates at that point.

Each of the three components of \widehat{T} are linear combinations of the $\Phi_{i,j,k}$'s:

$$\widehat{T} := \left(\sum \alpha_{i,j,k} \Phi_{i,j,k}, \sum \beta_{i,j,k} \Psi_{i,j,k}, \sum \gamma_{i,j,k} \Phi_{i,j,k} \right) \quad (2)$$

The coefficients $\alpha_{i,j,k}, \beta_{i,j,k}, \gamma_{i,j,k}$ are computed as the solution to a linear system:

$$(A^t A + \lambda_1 H^t H + \lambda_2 G^t G) \mathbf{x} = A^t \mathbf{b} \quad (3)$$

This linear system is equivalent to a optimization problem where

1. A and \mathbf{b} are chosen so that the linear system $A\mathbf{x} = \mathbf{b}$ expresses that \widehat{T} extends the deformable registration. More explicitly, for each vertex \mathbf{u} of the floating centerline network,

$$(\widehat{T} \circ \widehat{L})(\mathbf{u}) = (T \circ L)(\mathbf{u}) \quad (4)$$

2. H is the *graph Laplacian* (e.g. Godsil and Royle (2001)) of a Cartesian grid representation of the vessel wall, and the linear system $H\mathbf{x} = \mathbf{0}$ expresses that for each vertex \mathbf{p} on the vessel wall, $\widehat{T}(\mathbf{p})$ is the average value of $\widehat{T}(\mathbf{q})$ among the neighboring vertices \mathbf{q} of \mathbf{p} . Intuitively, this condition limits the strain imposed by \widehat{T} on the vessel wall.
3. G is a *Tikhonov* matrix (optionally the identity matrix) and the linear system $G\mathbf{x} = \mathbf{0}$ expresses that $\widehat{T} \equiv \mathbf{0}$. Intuitively, the displacement imposed by \widehat{T} is as small as possible.

These objectives are not simultaneously satisfiable but their relative importance in the optimization are prescribed by the ‘‘regularization’’ parameters λ_1, λ_2 in equation 3.

4. Results

MRA and 4D Flow images of a sample patient’s thoracic cavity were enhanced to highlight the aorta, brachiocephalic, left

carotid and left subclavian arteries. Centerlines were extracted from the enhanced MRA and the coherence image computed from the enhanced 4D Flow image. These centerline networks were registered using the polyline network registration algorithm described in Section 2. A corrected MRA was constructed using the algorithm in Section 3.

Surface representations of selected vessels were segmented from the MRA, corrected MRA and the coherence field of the 4D Flow image. These surfaces are illustrated in Figure 8.

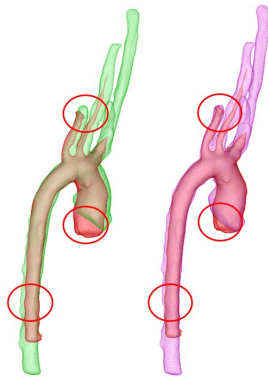


Fig. 8. Vessel surfaces segmented from the 4D Flow coherence image (red), the unregistered MRA image (green) and the registered MRA image (magenta)

Centerline networks of these vessels (distinct from the centerlines used in the curve registration step) were extracted from these surfaces/images. These centerline networks are illustrated in Figure 9.

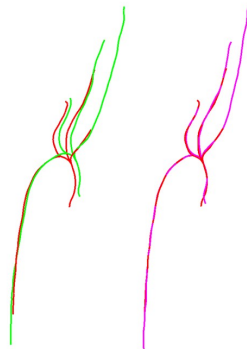


Fig. 9. Curves extracted from the 4D Flow coherence image (red), the unregistered MRA image (green) and the registered MRA image (magenta)

Reduced distance histograms between 4D Flow-derived centerlines and MRA-derived centerlines are illustrated in Figure 10.

Estimates of flux in the aorta using the 4D Flow image, uncorrected MRA image and corrected MRA image were computed and illustrated in Figure 11.

5. Conclusions

The surface plots (Figure 8) and histograms (Figure 10) attest to the improved alignment between the MRA and 4D Flow im-

ages resulting from the registration detailed in this paper. Additionally, the flux estimated from the registered and unregistered pair show the significant influence of the registration on blood flow properties of interest.

5.1. Discussion, Limitations and Future Work

5.1.1. Estimating flow properties solely from the 4D Flow image

Note, μ_j and ρ_i represent the same type (i.e. density) of information and can both be used to identify anatomical structures in their target domain. Moreover, μ_j is assumed to be aligned. The benefit of using ρ_i over μ_j , even at the cost of performing the entire registration, is the improved resolution, in practice, of MRA images over 4D Flow images.

It is possible to extract segmentations from the 4D Flow image v_j . One way is to compute the (scalar) coherence image and apply standard segmentation techniques. As mentioned earlier, such surfaces are biased and inaccurate. Some software generate surfaces from the 4D Flow images, but these surfaces also suffer from quality issues. See Punzo *et al.* (2023) and Oechtering *et al.* (2023).

The higher spatial resolution generally present in MRA images justifies the registration process to get accurate and aligned segmentations. See Figure 12.

5.1.2. Valid only for small misalignment/deformations

The registration can be extremely inaccurate if the misalignments/deformations of the original images are not sufficiently small. This limitation is very common among solutions to registration problems.

5.1.3. Locality

While the corrected MRA is designed to more closely agree with the 4D Flow image in the vicinity of the selected vessel network used to generate it, the corrected MRA is virtually unchanged (and hence not corrected) away from the vessels. Extending the vessel network, perhaps beyond those vessels whose blood flow properties are of interest, may alleviate this problem.

5.1.4. Direct registration of segmentations

Using the methods presented in this paper, segmentations of surfaces depicted in an MRA image that align with a given 4D Flow image can be obtained by extracting segmentations from the corrected MRA image. The construction of the corrected MRA itself may involve several segmentations, which require significant human effort.

In a common scenario, segmentations extracted from the uncorrected MRA exist before the corrected MRA construction is even initiated. A minor modification of the MRA correction algorithm produces aligned segmentations from the unaligned ones without constructing the entire corrected MRA thus avoiding the cost of producing additional segmentations.

Let $\{v_i\}$ be the vertices of a surface mesh segmented from an unregistered MRA. The vertices of the registered surface are then given by

$$(\widehat{L}^{-1} \circ \widehat{T})(v_i)$$

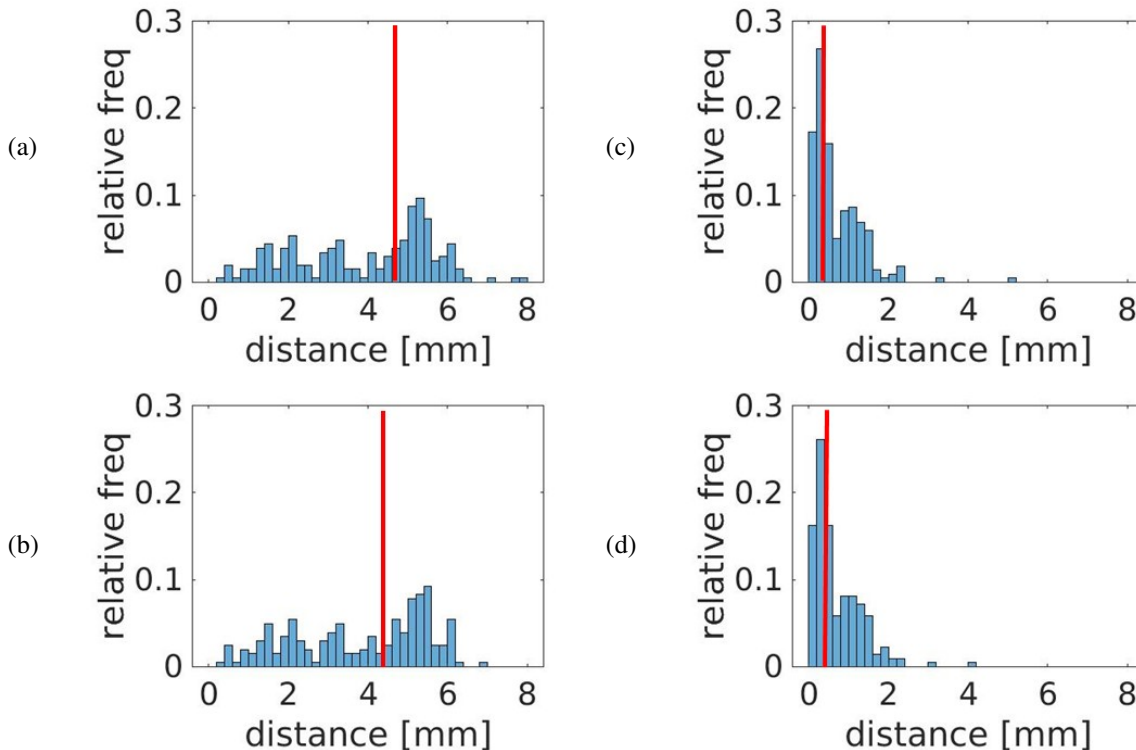


Fig. 10. Reduced asymmetric distance histograms with median distances indicated in red. (a) from fixed to floating centerline network (b) from floating to fixed centerline network (c) from fixed to registered centerline network (d) from registered to fixed centerline network.

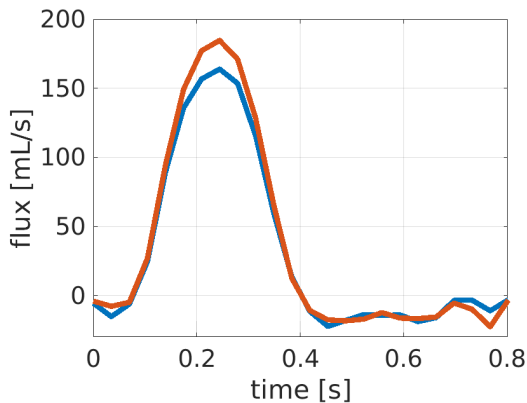


Fig. 11. Flow waveform at a cross-section of the descending aorta just downstream of the left subclavian artery. The red (blue) curve is computed from the aligned (unaligned) MRA images.

where \widehat{L} is the unique extension to \mathbb{R}^3 of the rigid transformation L and \widehat{T} is constructed as in the original method except for a single modification:

Equation 4

$$(\widehat{T} \circ \widehat{L})(\mathbf{u}) = (T \circ L)(\mathbf{u})$$

is replaced by

$$\widehat{T}((T \circ L)(\mathbf{u})) = L(\mathbf{u}) \quad (5)$$

With this modification, \widehat{T} should be understood as approxi-

mately extending T^{-1} instead of T .¹⁴

5.1.5. Automatic Centerline Extraction

The time required to process and register a pair of images with a naive software implementation of this algorithm is dominated by the time it takes for a user to extract centerlines from the MRA and (coherence of) 4D Flow images. Software tools for more automated extraction of centerlines (such as in Chadwick *et al.* (2021)) would certainly alleviate this problem. Moreover, it would reduce subjectivity and variability that human-controlled computations often contribute.

5.1.6. Tuning Parameters

As commonly plagues image processing algorithms, and signal processing algorithms in general, performance is affected by the specification of several parameters. Systematic methods or even heuristics for choosing these parameters are beyond the scope of this initial work.

5.1.7. Enriched Network Model

Curve networks, as they are currently modelled, are simply sets of curves with no representation of their topology. Enriching the network models with connectivity information and branch points may better inform the registration process and improve performance.

¹⁴This intuition is still appropriate in the rare cases that T is not invertible.

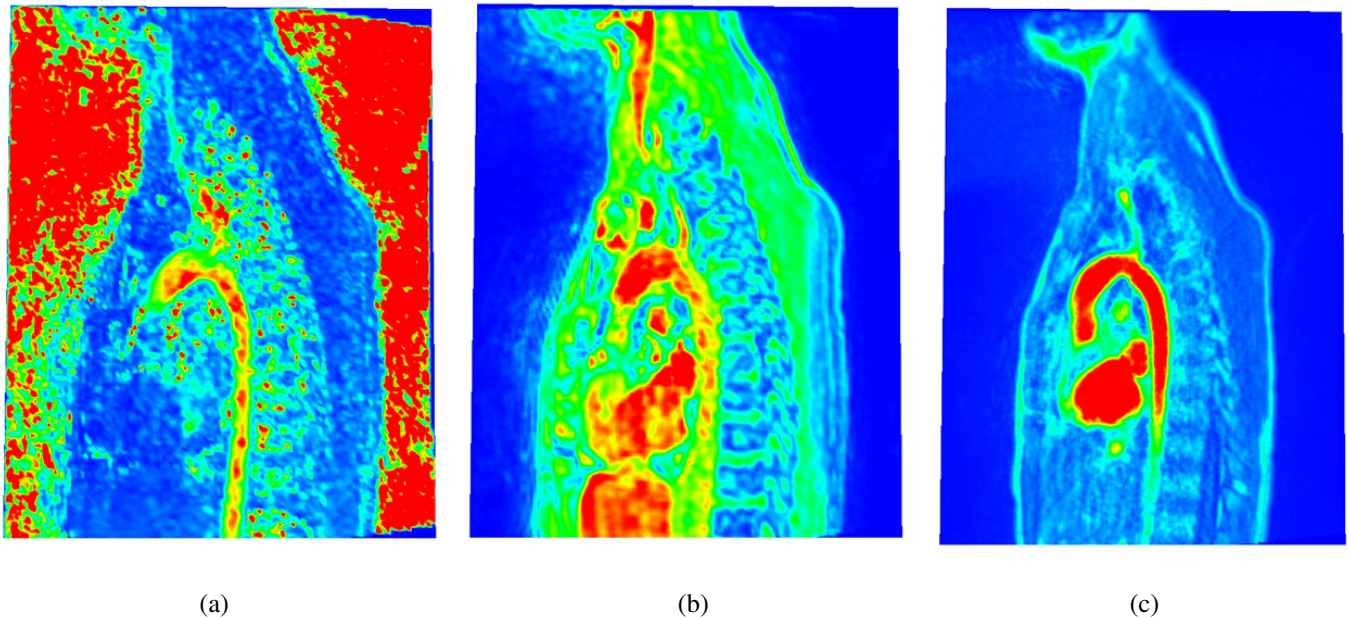


Fig. 12. Cross sections illustrate the differences in signal to noise ratio and resolution of the following scalar volumes: (a) velocity magnitude (from 4D Flow), (b) magnitude (from 4D Flow) and (c) density (from MRA).

Acknowledgments

This research did not receive any specific grant from funding agencies in the public, commercial, or not-for-profit sectors.

References

- Besl, P.J., McKay, N.D., 1992. Method for registration of 3-D shapes, in: Sensor fusion IV: control paradigms and data structures, SPIE. pp. 586–606. doi:10.1117/12.57955.
- Biglino, G., Giardini, A., Ntsinjana, H.N., Schievano, S., Hsia, T.Y., Taylor, A.M., Modeling of Congenital Hearts Alliance Collaborative Group, 2014. Ventriculoarterial coupling in palliated hypoplastic left heart syndrome: Noninvasive assessment of the effects of surgical arch reconstruction and shunt type. *J Thorac Cardiovasc Surg* 148, 1526–1533. doi:10.1016/j.jtcvs.2014.02.012.
- Biglino, G., Schievano, S., Steeden, J.A., Ntsinjana, H., Baker, C., Khambadkone, S., de Leval, M.R., Hsia, T.Y., Taylor, A.M., Giardini, A., Modeling of Congenital Hearts Alliance (MOCHA) Collaborative Group, 2012. Reduced ascending aorta distensibility relates to adverse ventricular mechanics in patients with hypoplastic left heart syndrome: noninvasive study using wave intensity analysis. *J Thorac Cardiovasc Surg* 144, 1307–13; discussion 1313–4. doi:10.1016/j.jtcvs.2012.08.028.
- Biko, D.M., Gaynor, J.W., Partington, S.L., Harris, M.A., Whitehead, K.K., Trusty, P., Yoganathan, A.P., Fogel, M.A., 2019. Relationship of aortic stiffness to exercise and ventricular volumes in single ventricles. *Ann Thorac Surg* 108, 574–580. doi:https://doi.org/10.1016/j.athoracsur.2019.03.019.
- Bruse, J.L., Cervi, E., McLeod, K., Biglino, G., Sermesant, M., Pennec, X., Taylor, A.M., Schievano, S., Hsia, T.Y., Modeling of Congenital Hearts Alliance (MOCHA) Collaborative Group, 2017. Looks do matter! aortic arch shape after hypoplastic left heart syndrome palliation correlates with cavopulmonary outcomes. *Ann Thorac Surg* 103, 645–654. doi:10.1016/j.athoracsur.2016.06.041.
- Bustamante, M., Petersson, S., Eriksson, J., Alehagen, U., Dyverfeldt, P., Carlhäll, C.J., Ebbers, T., 2015. Atlas-based analysis of 4D flow CMR: Automated vessel segmentation and flow quantification. *J Cardiovasc Magn Reson* 17. doi:10.1186/s12968-015-0190-5.
- Chadwick, E., Suzuki, T., George, M., Romero, D., Amon, C., Waddell, T., Karoubi, G., Bazylak, A., 2021. Vessel network extraction and analysis of mouse pulmonary vasculature via x-ray micro-computed tomographic imaging. *PLoS Comput Biol* 17. doi:10.1371/journal.pcbi.1008930.
- Fogel, M.A., Li, C., Nicolson, S.C., Spray, T.L., Gaynor, J.W., Fuller, S., Keller, M.S., Harris, M.A., Yoganathan, A.P., Whitehead, K.K., 2014. Comparison by magnetic resonance phase contrast imaging of pulse-wave velocity in patients with single ventricle who have reconstructed aortas versus those without. *Am J Cardiol* 114, 1902–1907. doi:10.1016/j.amjcard.2014.09.032.
- Godsil, C., Royle, G., 2001. Algebraic Graph Theory. Graduate Texts in Mathematics. 2001 ed., Springer, New York, NY. doi:10.1007/978-1-4613-0163-9.
- Gupta, V., Bustamante, M., Fredriksson, A., Carlhäll, C.J., Ebbers, T., 2018. Improving left ventricular segmentation in four-dimensional flow MRI using intramodality image registration for cardiac blood flow analysis. *Magn Reson Med* 79, 554–560. doi:10.1002/mrm.26674.
- Kikinis, R., Pieper, S.D., Vosburgh, K.G., 2013. 3D Slicer: a platform for subject-specific image analysis, visualization, and clinical support, in: Intraoperative Imaging and Image-Guided Therapy. Springer, pp. 277–289. doi:10.1007/978-1-4614-7657-3_19.
- Langer, T., Belyaev, A., Seidel, H.P., 2005. Analysis and design of discrete normals and curvatures URL: https://pure.mpg.de/rest/items/item_1819179/component/file_1840884/content.
- Oechtering, T.H., Nowak, A., Sieren, M.M., Stroth, A.M., Kirschke, N., Wegner, F., Balks, M., König, I.R., Jin, N., Graessner, J., Kooijman-Kurfuerst, H., Hennemuth, A., Barkhausen, J., Frydrychowicz, A., 2023. Repeatability and reproducibility of various 4D flow MRI postprocessing software programs in a multi-software and multi-vendor cross-over comparison study. *J Cardiovasc Magn Reson* 25, 22. doi:10.1186/s12968-023-00921-4.
- Punzo, B., Ranieri, B., Tramontano, L., Affinito, O., Franzese, M., Bossone, E., Saba, L., Cavaliere, C., Cademartiri, F., 2023. 4D-Flow Cardiovascular

- Magnetic Resonance Sequence for Aortic Assessment: Multi-Vendor and Multi-Magnetic Field Reproducibility in Healthy Volunteers. *J Clin Med* 12. doi:10.3390/jcm12082960.
- Sabokrohiyeh, S., Ang, K., Elbaz, M.S.M., Samavati, F.F., 2019. Sketch-based Registration of 3D Cine MRI to 4D flow MRI, pp. 14–21. doi:10.1145/3340074.3340094.
- Sang, Y., Cao, M., McNitt-Gray, M., Gao, Y., Hu, P., Yan, R., Yang, Y., Ruan, D., 2021. Enhancing 4d Cardiac Mri Registration Network With A Motion Prior Learned From Coronary Cta, in: 2021 IEEE 18th International Symposium on Biomedical Imaging (ISBI), pp. 917–920. doi:10.1109/ISBI48211.2021.9433819.
- Sang, Y., Cao, M., McNitt-Gray, M., Gao, Y., Hu, P., Yan, R., Yang, Y., Ruan, D., 2022. Inter-Phase 4D Cardiac MRI Registration With a Motion Prior Derived From CTA. *IEEE Trans Biomed Eng* 69, 1828–1836. doi:10.1109/TBME.2021.3127158.
- Schäfer, M., Younoszai, A., Truong, U., Browne, L.P., Mitchell, M.B., Jagers, J., Campbell, D.N., Hunter, K.S., Ivy, D.D., Di Maria, M.V., 2019. Influence of aortic stiffness on ventricular function in patients with Fontan circulation. *J Thorac Cardiovasc Surg* 157, 699–707. doi:10.1016/j.jtcvs.2018.09.039.
- Taylor-LaPole, A.M., Colebank, M.J., Weigand, J.D., Olufsen, M.S., Puelz, C., 2023. A computational study of aortic reconstruction in single ventricle patients. *Biomech Model Mechanobiol* 22, 357–377. doi:10.1007/s10237-022-01650-w.
- Updegrove, A., Wilson, N.M., Merkow, J., Lan, H., Marsden, A.L., Shadden, S.C., 2017. SimVascular: An open source pipeline for cardiovascular simulation. *Ann Biomed Eng* 45, 525–541. doi:10.1007/s10439-016-1762-8.